Article

Neuron

Neural Circuits Underlying Visually Evoked Escapes in Larval Zebrafish

Highlights

- Larval zebrafish escape from looming stimuli after a critical image size is reached
- Population activity of neurons in the optic tectum encodes critical image size
- Modeling predicts the critical role of characterized cell types in the retina and tectum
- Motor output is conveyed via multimodal circuitry in the hindbrain

Authors

Timothy W. Dunn, Christoph Gebhardt, Eva A. Naumann, Clemens Riegler, Misha B. Ahrens, Florian Engert, Filippo Del Bene

Correspondence

florian@mcb.harvard.edu (F.E.),
filippo.del-bene@curie.fr (F.D.B.)

In Brief

Dunn et al. characterize the parameters influencing visually evoked escape behavior in larval zebrafish. Via large-scale functional imaging, the authors identify the neural circuits underlying the behavior and provide a mechanistic model that incorporates newly classified neural response types.

Dunn et al., 2016, Neuron *89*, 613–628
February 3, 2016
http://dx.doi.org/10.1016/j.neuron.2015.12.021

CellPress

Neuron
Article

Neural Circuits Underlying Visually Evoked Escapes in Larval Zebrafish

Timothy W. Dunn,[1,2] Christoph Gebhardt,[3] Eva A. Naumann,[4] Clemens Riegler,[1,6] Misha B. Ahrens,[5] Florian Engert,[1,2,*] and Filippo Del Bene[3,*]
[1]Department of Molecular and Cellular Biology and Center for Brain Science, Harvard University, Cambridge, MA 02138, USA
[2]Program in Neuroscience, Department of Neurobiology, Harvard Medical School, Boston, MA 02115, USA
[3]Institut Curie, PSL Research University, INSERM, U 934, CNRS UMR3215, 26 rue d'Ulm, 75005 Paris, France
[4]Department of Neuroscience, Physiology & Pharmacology, University College London, London WC1E 6BT, UK
[5]Howard Hughes Medical Institute, Janelia Farm Research Campus, Ashburn, VA 20147, USA
[6]Department of Neurobiology, Faculty of Life Sciences, University of Vienna, Althanstrasse 14, 1090 Wien, Austria
*Correspondence: florian@mcb.harvard.edu (F.E.), filippo.del-bene@curie.fr (F.D.B.)
http://dx.doi.org/10.1016/j.neuron.2015.12.021

SUMMARY

Escape behaviors deliver organisms away from imminent catastrophe. Here, we characterize behavioral responses of freely swimming larval zebrafish to looming visual stimuli simulating predators. We report that the visual system alone can recruit lateralized, rapid escape motor programs, similar to those elicited by mechanosensory modalities. Two-photon calcium imaging of retino-recipient midbrain regions isolated the optic tectum as an important center processing looming stimuli, with ensemble activity encoding the critical image size determining escape latency. Furthermore, we describe activity in retinal ganglion cell terminals and superficial inhibitory interneurons in the tectum during looming and propose a model for how temporal dynamics in tectal periventricular neurons might arise from computations between these two fundamental constituents. Finally, laser ablations of hindbrain circuitry confirmed that visual and mechanosensory modalities share the same premotor output network. We establish a circuit for the processing of aversive stimuli in the context of an innate visual behavior.

INTRODUCTION

When confronted with threatening stimuli, organisms respond with stereotyped behavioral patterns that promote survival. The most fundamental of these behaviors is the escape response, which delivers the individual away from assault. While these escapes are diverse across phyla (Chalfie et al., 1985; Muijres et al., 2014; Sherrington, 1910), they are nevertheless highly conserved and occupy an ancient and essential corner of the ethogram. Indeed, when examined ontogenetically, escape behaviors typically develop before the organism can feed or make coordinated movements (Armstrong and Higgins, 1971), highlighting the vital importance of these avoidance programs.

The robustness and stereotypy of escape behaviors are of great utility for studies of sensorimotor computations (Dickinson and Moss, 2012; Eaton et al., 2001; Fotowat and Gabbiani, 2011; Korn and Faber, 2005). Historically, studies of escape behaviors have often focused on impulse-like mechanosensory stimulation such as a touch or brief auditory buzz, where stimulus control and behavioral execution are straightforward and where the underlying sensory detection and processing pathways are relatively compact. The visual system, however, is arguably better suited for detecting threatening stimuli, as visual cues can be detected long before the mechanical signatures of an approaching predator reach somatosensory and auditory systems (Billington et al., 2011; Fotowat et al., 2011; Khakhalin et al., 2014; Oliva et al., 2007; Preuss et al., 2006; Yilmaz and Meister, 2013). At the same time, the sensory computations required for the visual detection of threats are potentially more complex, as these must involve the rapid analysis of high-dimensional spatiotemporal sensory streams. Nonetheless, mechanisms of visual escape behavior, typically evoked by signatures of impending collision (looming), have not been well studied outside of invertebrates (Gabbiani et al., 1999; von Reyn et al., 2014). Here, we use the behavioral, optical, and genetic accessibility of the larval zebrafish, *Danio rerio*, to address the neural basis of visually evoked escapes in a vertebrate animal.

In response to acoustic or tactile stimulation, larval zebrafish perform a fast, high-angle, stereotyped escape maneuver (the "C-bend") that is conserved across most anamniotes (Eaton et al., 2001). This escape behavior is recruited by a short ipsilateral arc (minimum two synapses) from the ear (in the case of sound) to rhombomere 4 of the hindbrain, where a premotor system dominated by the large, morphologically distinct Mauthner cell (M-cell) effects a high-amplitude turn to the contralateral side. While it is not known in zebrafish whether the M-cell and its associated segmental homologs (collectively, the M-system) mediate any visually guided behaviors, studies in goldfish (Preuss et al., 2006; Zottoli et al., 1987) show that the M-cell may receive visual input from the optic tectum (OT), the homolog of the mammalian superior colliculus.

In turn, a large body of evidence supports a role for the OT in complex visual processing. The OT, by far the largest contiguous larval visual brain structure, is recurrently connected across its laminar architecture and receives direct input from the majority

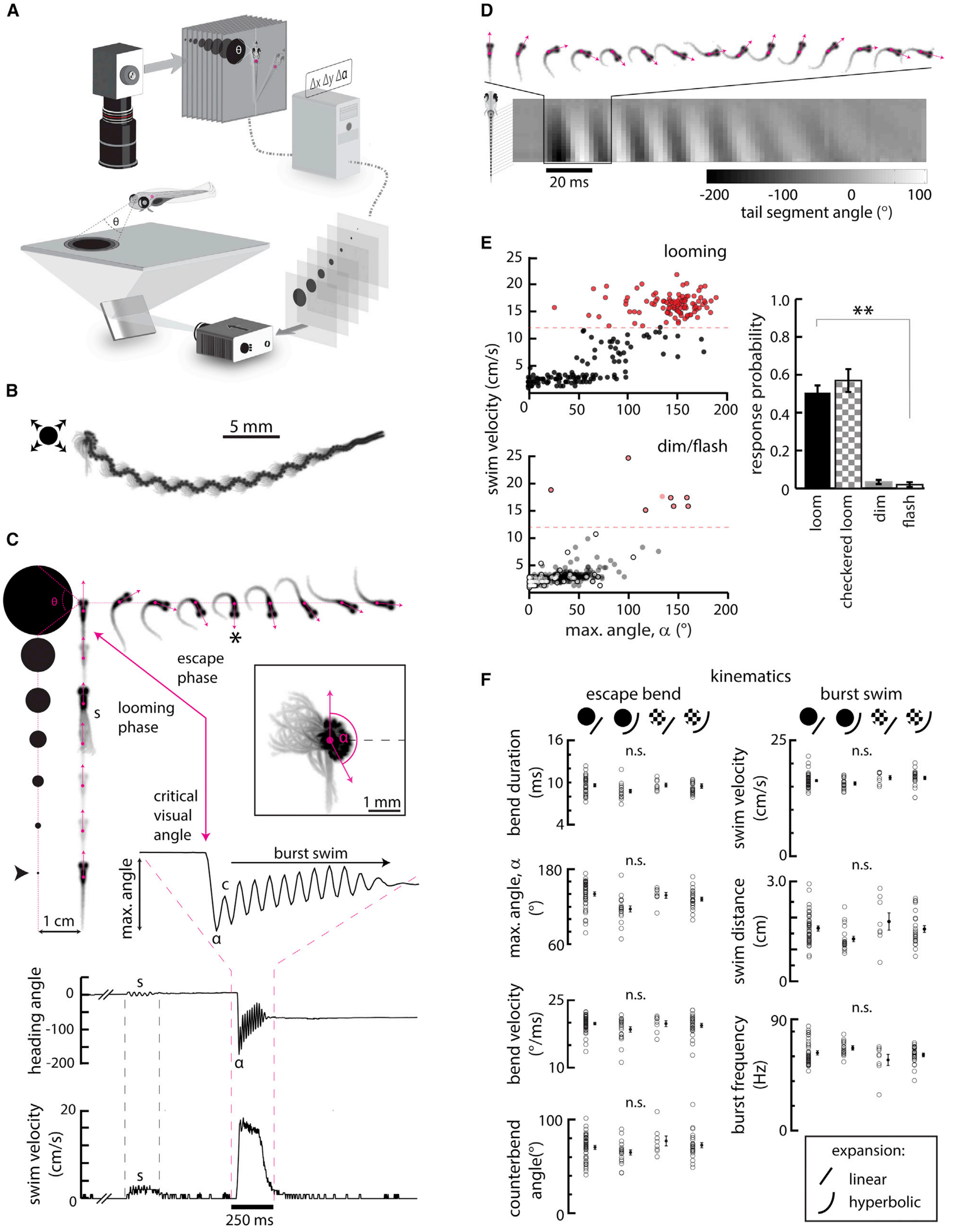

(legend on next page)

of retinal projections (Burrill and Easter, 1994) in addition to indirect input from accessory visual areas (Vanegas and Ito, 1983). Neurons in the OT show direction, orientation, speed, and size selectivity (Gabriel et al., 2012; Grama and Engert, 2012; Hunter et al., 2013; Niell and Smith, 2005) and respond to aversive (predator-like) and appetitive (prey-like) visual cues in many animals (Dean et al., 1989; Ewert, 1997; Muto et al., 2013). Furthermore, OT neurons in birds (Winkowski and Knudsen, 2008), tadpoles (Khakhalin et al., 2014), frogs (Baranauskas et al., 2012), and fish (Niell and Smith, 2005) respond to looming stimuli. Thus, the OT is well positioned to mediate visually evoked escape responses by feeding filtered visual input to the hindbrain M-system and associated escape circuitry.

However, so far, a causal link between the hindbrain M-system and visually evoked escapes has not been demonstrated. Furthermore, most analyses of tectal processing have remained descriptive and treat single cells in isolation (Gabriel et al., 2012; Grama and Engert, 2012), independent of behavior and the activity of other visual, motion-sensitive midbrain structures such as the pretectum (Kubo et al., 2014; Portugues et al., 2014). Given its anatomical and functional position, an understanding of population activity in the OT during a well-defined visuomotor behavior would lead to new insights into how the vertebrate central nervous system isolates behaviorally relevant cues from sensory streams and transforms these into behavior.

In this study, we employ a combination of behavioral and calcium imaging techniques to map the sensory and motor systems underlying visually evoked escape behavior and construct a working model of behaviorally relevant stimulus representation in the OT. We establish that freely swimming larval zebrafish respond to visual stimuli representing object approach with directed C-bend escape maneuvers and describe a convergence in the circuits mediating mechanosensory and visual escapes at the premotor level. In addition, we demonstrate that the OT encodes the critical image size associated with escape latency across hundreds of periventricular neurons (PVNs), providing a novel basis for ethologically relevant processing in collicular structures. Furthermore, we measure the activity in the presynaptic terminals of retinal ganglion cells that provide the input to the OT as well as the response properties of superficial inhibitory interneurons (SINs) that have been shown to serve as important computational units in the context of separating large from small moving objects (Del Bene et al., 2010). These data allow us to propose a mechanistic model of how the behaviorally relevant dynamics of PVNs—the putative output neurons of the OT—arise in the context of looming stimuli. Together, these results outline the circuitry and computations controlling a robust, innate visually guided behavior and reveal fundamental principles of neural system organization likely prevalent in subcortical visual structures across phyla.

RESULTS

Looming Visual Stimuli Evoke Fast Escape Maneuvers in Larval Zebrafish

To test how larval zebrafish respond to looming stimuli, we constructed an arena in which individual freely swimming fish were monitored with a high-speed camera while visual stimuli were presented with closed-loop feedback onto a screen beneath the animal (Figure 1A). This high-speed (506 fps acquisition,

Figure 1. Kinematic Analysis of Looming-Specific Escapes

(A) Schematic of the closed-loop behavior setup used to present visual stimuli and monitor behavior. Video is analyzed online to detect fish position and orientation in real time. This information is used to update stimulus position with closed-loop feedback so that stimuli remain in a fixed position within the fish's visual field.

(B) The trajectory of a single looming-evoked behavioral response, shown here as the multiple movie frames superimposed (106 frames, 210 ms). An expanding, looming disk presented in the left visual field evokes a high-angle, long-distance maneuver to the right. In this representation, the eyes and swim bladder appear as dark spots, and the gray shades are the tail.

(C) Each individual trial can be separated into a looming phase (fish images, bottom to top), where the stimulus expands while locked to a fixed position from the fish center of mass (frames separated by 250 ms to illustrate dynamics; black arrowhead denotes stimulus start time), and an escape phase (fish images, top, left to right), during which the fish executes a high-angle, high-velocity escape maneuver (frames separated by the true frame period, 1.98 ms at 506 fps). Heading direction (pink vectors) and center of mass (pink dots) are extracted from each frame and used to characterize behavioral responses. (s) shows a spontaneous swim bout that occurs before this fish initiates an escape response (shown here as multiple superimposed movie frames), illustrating the need for closed-loop stimulus presentation. The same event is marked in the heading angle and swim velocity plots below. The asterisk (*) represents the frame corresponding to the maximum change in heading direction (inset and time series, angle α). Bottom plots are of heading angle and instantaneous swim velocity isolated from video. A zoom-in of heading direction reveals a high-angle bend followed by a small counterbend (c) and a high-frequency burst swim lasting hundreds of milliseconds.

(D) An example of a looming-evoked escape with a large counterbend. The angle of 20 equally spaced points along the tail relative to the fish body axis can be extracted from high-resolution video, revealing detailed tail kinematics.

(E) Top left shows a scatterplot of maximum heading angle change, α, and swim velocity for all swim events initiated during looming stimulus presentation (N = 37 fish; n = 315 swim events). Bottom left shows a scatterplot for all swim events initiated while presenting dimming (filled circles, N = 26, and n = 116) or flashed (open circles, N = 10, and n = 1,097) stimuli. Red depicts high-angle, high-velocity swim events above a threshold maximum swim velocity of 12.0 cm/s (dashed red line). Right shows a quantification of escape response probability across multiple stimulus conditions. For this responsivity analysis, fish were included only if they responded at least once to at least one stimulus in the stimulus set. Looming black (N = 33 fish) and checkered (N = 8) spots elicit escape-like maneuvers much more often than dimming (N = 27) or flashed (N = 6) stimuli. Looming stimuli expanded with constant radial velocity (linear expansion). Error bars represent mean ± SEM across fish. $^{**}p < 10^{-5}$, permutation test.

(F) Analysis of seven kinematic variables across four different classes of looming stimuli that vary in either radial expansion dynamics (linear or hyperbolic) or relative contrast (black or checkered isoluminant). Left panels depict kinematics associated with the initial high-angle bends (α) of classified escapes. Right panels show kinematics associated with the burst swim phase of behavioral responses. While expansion dynamics may affect kinematics slightly, all variables are statistically similar across all four conditions after applying the Bonferroni correction ($[\text{significance level}]_{0.05}/7 \approx 0.007$; p = 0.008 maximum angle, p = 0.199 bend duration, p = 0.241 bend velocity, p = 0.086 swim distance, p = 0.077 burst frequency, p = 0.125 swim velocity, and p = 0.175 counterbend angle, F-statistic [ANOVA] permutation test). Offset points and error bars are mean ± SEM across fish. Each open circle is the mean for a single fish. N = 49 fish, n = 301 responses, black linear expansion; N = 19, n = 192, black hyperbolic expansion; N = 8, n = 65, checkered linear expansion; N = 25, n = 322, checkered hyperbolic expansion.

60 Hz stimulus update), closed-loop stabilization generated maximal consistency in visual stimulation across presentations; furthermore, locked egocentric stimuli best matched the conditions used in subsequent imaging experiments.

Looming dark spots, which mimic approaching objects or predators (Gabbiani et al., 1999), were presented on a neutral gray background to 5- to 6-days-post-fertilization (dpf) larvae. These spots started at singular points offset orthogonally from the fish midline and expanded as disks with either constant radial velocity (linear expansion) or constant approach velocity (hyperbolic expansion), the former corresponding to a decelerating approach. Stimuli were presented either to the left or right side of the animal, remaining exclusively within each respective monocular visual field (Bianco et al., 2011) for at least the first half of the expansion period. These looming stimuli typically evoked high-velocity, high-angle, long-distance swim maneuvers (Figures 1B and 1C; Movie S1) that we quantified using detailed kinematic analysis (Figure 1D).

To better distinguish looming-evoked escape responses from other maneuvers in the larval zebrafish behavioral repertoire (e.g., routine turns or spontaneous swimming), we plotted the maximum instantaneous linear velocities and bend angles of all locomotion events initiated after stimulus onset but before the stimulus had stopped expanding. This analysis revealed a cluster of high-velocity, high-angle events separated from routine turns and swimming, demonstrating that looming stimuli consistently evoke escape-like responses that are distinct from other behaviors (Figure 1E). To probe whether these responses were indeed specific to looming stimuli, we also presented spots that appeared instantaneously (flashed stimuli) or spots that dimmed with the same temporal dynamics as the looming stimuli. A response probability metric—the probability of maximum swim velocity exceeding 12.0 cm/s (Figures S1A–S1C)—indicated looming-stimuli-induced escapes about half of the time (51.0 ± 3.8% for linear expansion, and 46.0 ± 9.3% for hyperbolic expansion), whereas high-velocity escape maneuvers almost never occurred during presentation of dimming and flashed stimuli (3.4 ± 1.1% and 2.0 ± 1.3%, respectively).

To test in more detail which stimulus feature generated the escape behavior during looming stimulus presentation, we evaluated whether object expansion was the key trigger. Expanding disks decrease overall luminance; although larvae did not escape to dimming alone, it is possible that a conjunction of looming and dimming is required for triggering escapes. Therefore, we presented checkered looming stimuli (Fotowat and Gabbiani, 2007), which were subjectively isoluminant over the time course of expansion. These stimuli were equally efficacious in evoking escape responses (57.0 ± 6.1% of the time for linear expansion; Figure 1E; and 60.2% ± 4.7% for hyperbolic expansion), providing further evidence that this behavior employs complex, luminance-independent visual computations to detect expanding borders, consistent with looming-evoked escape responses in other species (Gabbiani et al., 2001; Landwehr et al., 2013; de Vries and Clandinin, 2012).

Zebrafish escape behavior has so far been described primarily in the context of mechanosensory C-starts (Burgess and Granato, 2007a; Gahtan et al., 2002; Kohashi and Oda, 2008; Liu and Fetcho, 1999; O'Malley et al., 1996), which are characterized by stereotyped kinematics. To better define looming-evoked behavior and compare it to these C-start escapes, we analyzed seven different kinematic variables across four looming stimulus conditions: black or checkered constant radial expansion and black or checkered hyperbolic expansion. While the former pair simulated a decelerating approach trajectory, the latter pair simulated object approach at constant velocity, the stimulus most commonly used in other organisms (Hatsopoulos et al., 1995). We found that most kinematic variables tested were indistinguishable across the four stimuli with the exception of maximum bend angle, which varied slightly depending on the temporal dynamics of expansion (Figure 1F). Applying the Bonferroni correction (Dunn, 1961) for multiple comparisons, however, eliminates this significance. Thus, all four types of looming stimuli trigger indistinguishable motor programs.

Across all stimulus conditions, looming-evoked behaviors are characterized by at least three unique phases. First, larvae initiated a rapid (bend duration 9.4 ± 0.1 ms; maximum bend velocity 19.5 ± 0.2°/ms), high-angle bend (133.4 ± 2.1°) that quickly reverses heading direction. Second, fish performed a counterbend that re-oriented the body (70.4 ± 1.3°). Third, fish executed a high-velocity burst swim (velocity 16.4 ± 0.2 cm/s; burst (undulation) frequency 62.7 ± 0.9 Hz) away from the starting position (distance 1.5 ± 0.1 cm, mean ± SEM across fish). These kinematics closely resemble the C-start escape behaviors elicited by mechanosensory modalities (Figures S1D–S1F) (Budick and O'Malley, 2000; Eaton et al., 1988) and are starkly different from the high-angle dark flash o-bend (Burgess and Granato, 2007b; Huang et al., 2013) or large spot avoidance (Bianco et al., 2011) behaviors previously described. Thus, this response to looming stimuli is the first detailed description of a rapid escape behavior elicited by a visual stimulus in freely swimming larval zebrafish.

Escape Trajectories Are Dictated by Stimulus Position within the Visual Field

The directionality of escape can often be influenced by the location of the eliciting stimulus, reflecting an obvious but important strategy to effectively distance oneself from threats. Touch-evoked escapes in larval zebrafish are coarsely directional (Kohashi et al., 2012), and looming-evoked behaviors in locusts (Santer et al., 2005), flies (Card and Dickinson, 2008), and adult goldfish (Eaton and Emberley, 1991) show a dependence on incident angle. To probe whether looming-evoked behavior in larval zebrafish is influenced by stimulus position, we compared the escape trajectories elicited by looming stimuli presented in fixed positions in either the front, back, right, or left visual field (0°, 180°, 270°, and 90° relative to the fish center of mass, respectively). In 33 fish, stimuli in the right visual field consistently evoked escapes to the left, and vice versa. This relationship is readily identifiable when escape trajectories are rotated and aligned onto the body axis for each condition (Figure 2A). Despite differences in escape direction (Figure 2B, angular histograms), the velocity of escape maneuvers is similar across all conditions, as evidenced by plots of fish position 50 ms after escape initiation (Figure 2B). Quantification of response preference across fish formalizes a strong positional dependence for left and right stimuli (0.68 ± 0.09 and −0.69 ± 0.09 preference index, respectively) and a lack of directional bias for binocular front and back

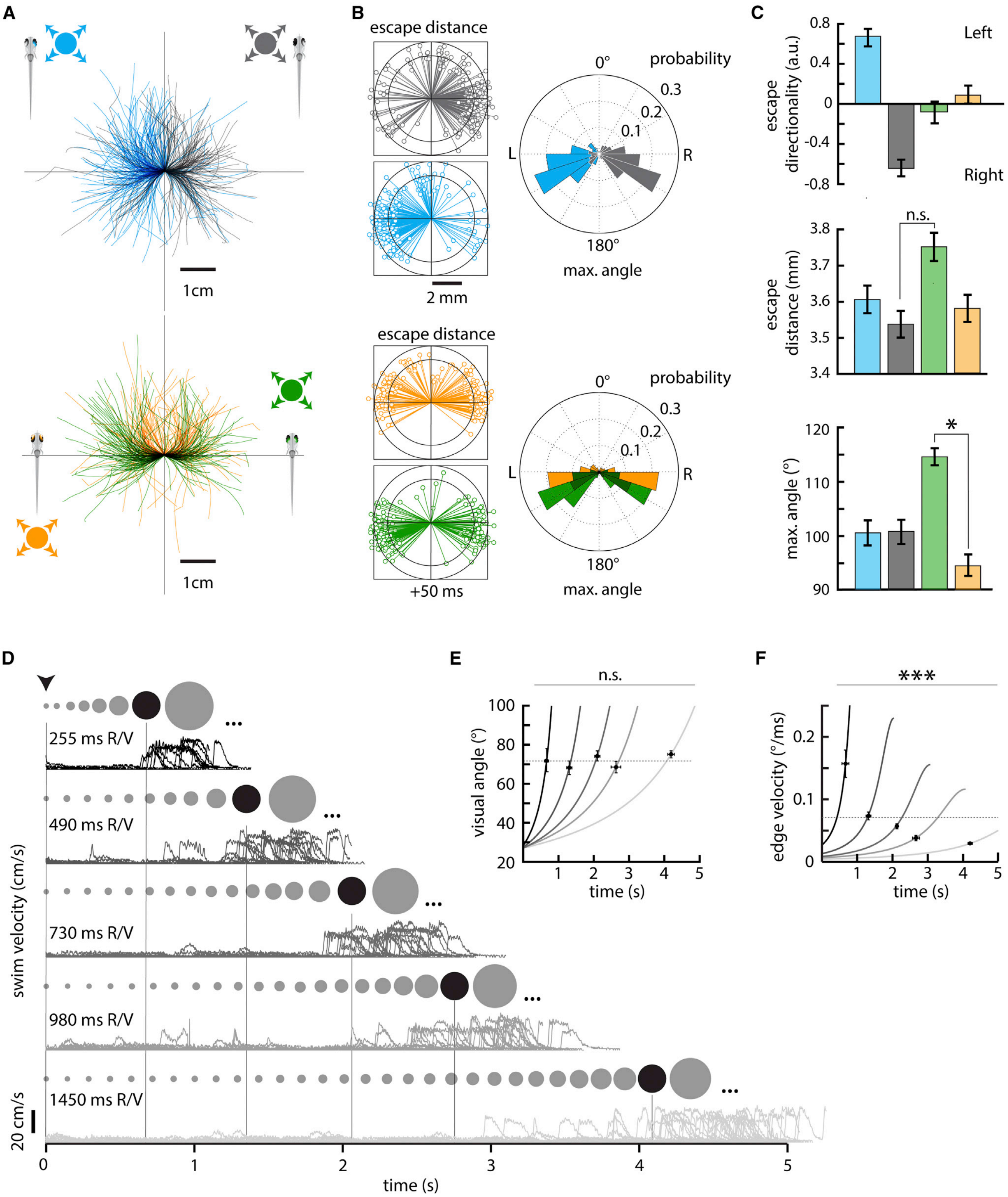

Figure 2. Stimulus Position and Dynamics Dictate Escape Direction and Latency

(A) Top panel shows escape trajectories elicited by looming dark spots in the right (blue, N = 34 fish, and n = 214 events) or left (black, N = 33, and n = 198) visual field. Bottom panel shows escape trajectories elicited by looming dark spots centered in the nasal [back] (orange, N = 21, and n = 164) or temporal [front] (green, N = 23, and n = 177) visual field.

(legend continued on next page)

stimuli (−0.14 ± 0.11 and 0.10 ± 0.10 preference index, respectively) (Figure 2C). Further analysis reveals that the observed trajectory bias reflects differences in absolute maximum turn angle (100.5° ± 2.3° for left, 100.7° ± 2.2° for right, 114.6° ± 1.5° for front, and 94.5° ± 2.0° for back stimuli), with back stimuli eliciting significantly shallower (smaller turn angle) responses ($p = 0.002$, permutation test). As indicated, the distance traveled by larvae after 50 ms does not depend on stimulus position (3.61 ± 0.04 mm for left, 3.54 ± 0.04 mm for right, 3.75 ± 0.04 mm for front, and 3.58 ± 0.04 for back stimuli; back, front $p = 0.127$, permutation test). It is worth noting that even in response to the same stimulus type, individual trajectories are highly variable; this suggests that larvae might employ a protean evasion strategy (Domenici et al., 2008; Humphries and Driver, 1970) that makes it harder for predators to predict and foil escapes once they are triggered. Nevertheless, these data demonstrate that larvae utilize a sensorimotor transformation that conserves positional stimulus information and alters escape motor programs accordingly.

Escapes Are Triggered When Stimuli Reach a Critical Visual Angle

To probe the effect of stimulus expansion velocity on visually evoked escape behaviors, we next presented a set of five stimuli that mimicked disks of constant radius approaching larvae from below at different velocities. When projected onto a flat surface, these stimuli can be described by functions of spot radius over time arising from fixed ratios of simulated disk radius and approach velocity (R/V; Figure S2) (Hatsopoulos et al., 1995). Escape latency was strongly modulated by stimulus velocity, with faster stimuli reliably eliciting escapes with shorter latencies (Figure 2D). When functions of stimulus image size and edge velocity are evaluated at times of escape onset (minus a fixed processing lag, $\Delta t = 81$ ms; see Experimental Procedures), an average threshold in angular image size (72.0° ± 1.3°, mean ± SEM across all 5 velocity conditions; $p = 0.198$, and F-statistic [ANOVA] permutation test; Figure 2E), but not edge velocity (Figure 2F), emerges ($p < 10^{-5}$, F-statistic [ANOVA] permutation test). This result is similar to descriptions of looming-evoked escape behaviors in other organisms (Fotowat and Gabbiani, 2007) and suggests that the circuits processing looming stimuli may primarily use stimulus size information when determining when and if an escape should be initiated.

Looming Stimuli Are Primarily Represented in the Optic Tectum

Our classification of looming-evoked escape behavior allowed us to explore the representation of this novel and ethologically relevant stimulus across various visual brain regions using calcium imaging in pan-neuronal *Tg(elav3:GCaMP5G)* 5- to 6-dpf larvae (Figure 3A) (Ahrens et al., 2013). To this end, larvae were fully embedded in agarose and imaged with a two-photon laser scanning microscope during stimulus presentation (Ahrens et al., 2012) to screen neurons for response selectivity. Looming stimuli and flashed stimuli evoked responses throughout the midbrain, which we segregated into three main regions based on anatomical boundaries and functional similarities: the OT, the pretectum/thalamus (PT/TH), and the midbrain tegmentum (MB) (Figure 3B). Responses to stimuli were diverse but, within the scope of this experiment, were categorized based only on significant differences in activity during looming and flashed stimulus epochs compared to baseline (see Experimental Procedures). This reduction allowed us to analyze stimulus selectivity, an indicator of processing specificity, throughout visual processing regions.

To quantify the anatomical distribution of looming-selective neurons across brain regions and fish, we mapped active neurons to a standard fish brain (Ahrens et al., 2012) after assigning a loom/flash selectivity index (SI; $[z_{\text{loom}} - z_{\text{flash}}]/[z_{\text{loom}} + z_{\text{flash}}]$; see Experimental Procedures) that effectively classified neural responses, with more positive values reflecting greater looming selectivity (Figure 3C). This analysis revealed a preponderance of looming-selective neurons in the ventral OT compared to the other midbrain regions we analyzed (Figure 3D). Furthermore, looming-selective activity in the OT typically peaked prior to the end of expansion, consistent with the timing of escape initiations (see examples in Figure 3B). On average, the OT was more than twice as selective as PT/TH or MB (0.35 ± 0.01, 0.17 ± 0.01, 0.11 ± 0.01 SI, respectively; OT, PT/TH $p < 10^{-5}$; OT, MB $p < 10^{-5}$, permutation test) and contained almost twice as many responsive neurons per unit volume (3.13 ± 0.40, 1.51 ± 0.28,

---

(B) Left panels show radial plots of fish position 50 ms after escape initiation. Right panels show angular histograms of the maximum turn angle (derived from orientation change, see Experimental Procedures) for all events in (A).

(C) Quantification of behavior across all four stimulus positions. The top bar plot depicts left-right preference [(# left turns − # right turns)/(# left turns + # right turns)] for right (blue, N = 26), left (gray, N = 26), back (orange, N = 18), and front (green, N = 17) stimuli for fish with at least five escape responses. Left and right stimuli consistently evoke responses directed away from the starting stimulus position, whereas back and front stimuli evoke responses to the left and right with near-equal probability. Error bars are mean ± SEM across fish. The middle bar plots depict mean distance traveled after 50 ms. The bottom bar plot shows mean maximum turn angle across all four conditions. $^{*}p < 0.001$, permutation test. Error bars are mean ± SEM across events.

(D) Records of swim velocity over time for escapes elicited by stimuli simulating approach at five different velocities (255 ms, 490 ms, 730 ms, 980 ms, and 1,450 ms R/V, top to bottom). The ratio R/V is a unique identifier of expansion trajectory (visual angle = $\theta(t) = 2^{*}\arctan(R/(-Vt))$, $t \leq 0$, where t is time to simulated collision). The spots above each trace schematize the size of the looming stimulus before a critical size is reached (dark spot), after which an escape is initiated with a fixed delay. Stimuli continue to expand (ellipses) until the end of the allotted trial time.

(E) Plots of visual angle (solid lines, velocity decreasing from left to right) evaluated at the average response latency for each velocity condition (crosses). The visual angle subtending the axis of the stimulus parallel to the fish body axis 81 ms before escape initiation is not significantly different across all five conditions. We determined the fixed delay ($\Delta t = 81$ ms) by minimizing the threshold visual angle standard deviation across all trials (see Experimental Procedures).

(F) Plots of edge velocity, $\dot{\theta}(t)$, evaluated at the average response latency for each velocity condition (crosses). Stimulus edge velocity 81 ms before escape initiation is significantly different across stimulus conditions ($^{***}p < 10^{-5}$, F-statistic [ANOVA], permutation test). Dotted lines represent the mean visual angle or edge velocity 81 ms prior to escape initiation across all conditions. For 255 ms R/V, N = 9, and n = 11; 490 ms, N = 12, and n = 20; 730 ms, N = 18, and n = 25; 980 ms, N = 19, and n = 31; 1,450 ms, N = 21, and n = 41. Error bars are mean ± SEM across events.

1.84 ± 0.32 active neurons per 1,000 μm^3, respectively; OT, PT/TH p = 0.001; OT, MB p = 0.010, permutation test). Furthermore, responses in the OT were also lateralized (Movie S2), with neurons in the left OT responding to looming stimuli in the right visual field and vice versa, consistent with the contralateral segregation of retinal streams and providing a putative mechanism for the observed lateralization of escape trajectory. These results suggest that the OT serves as a primary nucleus involved in looming detection within the larval zebrafish brain.

Population Activity Encodes Critical Image Size during Looming

If the OT is fundamentally involved in looming processing, activity in the OT should reflect the input-output relationships observed in freely swimming fish. To test this, we presented a set of looming stimuli expanding at three different R/V ratios (545 ms, 1,090 ms, and 2,730 ms) while imaging neural responses in the PVNs of the ventral OT.

Like ventral OT responses to constant radial expansion, activity in ventral OT neurons typically peaked prior to the end of expansion under different velocity conditions (Figures 3E, top, and S3C). The timing of these peaks relative to stimulus onset, however, was strongly influenced by expansion velocity, with responses to the slowest stimulus peaking nearly 8 s after responses to the fastest; this trend was reminiscent of the velocity-latency relationship we observed in freely swimming fish (Figure 2D). In order to better evaluate this correspondence, we performed principal component analysis to provide an unbiased estimate of looming representation across the OT neuronal population.

After aligning convolved stimulus size over time with the temporal evolution of the first principal component (temporal principal component, TPC1), which explained between 44% and 82% of the neural response variance (Figures S3A and S3B), a clear link between TPC1 and stimulus size is revealed (Figure 3E, bottom). Across all three velocity conditions, the OT population signals a common average angular image size (66.0 ± 4.5°, mean ± SEM across n = 23 TPC1 datapoints reaching threshold (of a possible 30) from 10 fish, 1,816 neurons, dotted black line in Figure 3F, left; see Experimental Procedures; p = 0.955, one-way ANOVA; compare to Figures 2D and 2E) during expansion as its activity crosses a fixed threshold (81% of the normalized peak TPC1 across stimuli; see Experimental Procedures). In order to estimate the visual angle signaled by TPC1, which reflects activity convolved with indicator dynamics that temporally shift underlying representations, this analysis was performed using convolved stimulus variables (GCaMP5G kernel, τ = 962 ms; Chen et al., 2013); a similar threshold angular image size is found when relating deconvolved TPC1 dynamics to raw visual angle (64.9° ± 5.0°; Figure S3D). This threshold angular image size represented by the OT population is in close agreement with the critical image size found to trigger the behavior in freely swimming experiments (72.0° ± 1.3°). Also similar to the behavior, TPC1 does not reach a threshold at a coherent edge velocity (Figure 3F, right). These data argue that the OT is capable of encoding a critical looming visual angle as an ensemble, providing an example of a putative mechanism for salient expansion encoding across a collicular population.

Retinal Ganglion Cell Terminals and SINs in the OT Encode Diverse Features of Looming Stimuli

In order to dissect the role of individual neural components of tectal circuitry in generating the population activity encoding critical angle, we analyzed activity patterns in two distinct neural cell types: retinal ganglion cells (RGCs) that send axons into the four input layers of the OT (SO, SFGS, SGC, and SAC; Nikolaou et al., 2012), and SINs, which have been shown to play a significant role in filtering out large (Del Bene et al., 2010) as well as small (Preuss et al., 2014) moving visual stimuli. In order to measure activity in RGC terminals, we generated a transgenic fish line (UAS:SyGCaMP6s) in which GCaMP6s (Chen et al., 2013) is linked to synaptophysin, and expression in RGCs is driven by an Isl2b:Gal4 line (Figure 4A) (Nikolaou et al., 2012). Presentation of looming stimuli at three different approach speeds revealed diverse dynamics in RGC terminals. Using a regression-based clustering approach (see Experimental Procedures; Bianco and Engert, 2015), we identified four major clusters capturing distinct properties of the rapidly evolving looming stimuli (Figure 4B). Notably, none of these clusters sufficiently match the population activity signatures extracted from the PVN population (see Figure 5), arguing that further processing occurs between retinal OT inputs and downstream PVNs.

In order to isolate putative processing units within the OT that might transform RGC inputs into the observed PVN population responses, we used a previously described line expressing nuclearly localized GCaMP6s (Freeman et al., 2014) under the elavl3 promoter, which, among other tectal neurons, also labels the SIN population. In this line, SINs are easily separated from other neurons in the OT because they are spatially segregated within neuropil layers (Figure 4C). Regression-based cluster analysis identified three main SIN response types, characterized by SIN responses to looming stimuli of different speeds (Figure 4D).

Non-linear Regression Identifies Two SIN Response Types as Potential Computational Modules Honing RGC Input in the OT

We next tested whether one or several of the SIN response types are sufficient to generate the signals recorded in the PVNs when they are allowed to operate on the input signals arriving in the OT via RGC projections. Figure 5A shows the four deconvolved RGC response types overlaid on the deconvolved average trace of the primary PVN response type extracted via cluster analysis (Figure S4); we focused on this PVN cluster because its activity appeared to shape TPC1 almost exclusively (Figure S4). It is clear that there is no perfect overlap between the PVN response and any of the RGC responses. The presence of well-characterized, wide-field GABAergic inhibitory interneurons (SINs) operating on the excitatory RGC inputs, however, suggested that the PVN population might inherit its response profile in a manner consistent with invertebrates, where excitatory and inhibitory inputs are non-linearly combined to create receptive fields that encode critical angle (Gabbiani et al., 1999). To ask whether a similar model, using excitation from RGCs and inhibition from SINs, might explain PVN responses, we tested pairwise combinations of RGC and SIN response types using a non-linear regression analysis (Figure 5B). Across all pairs, four show significantly

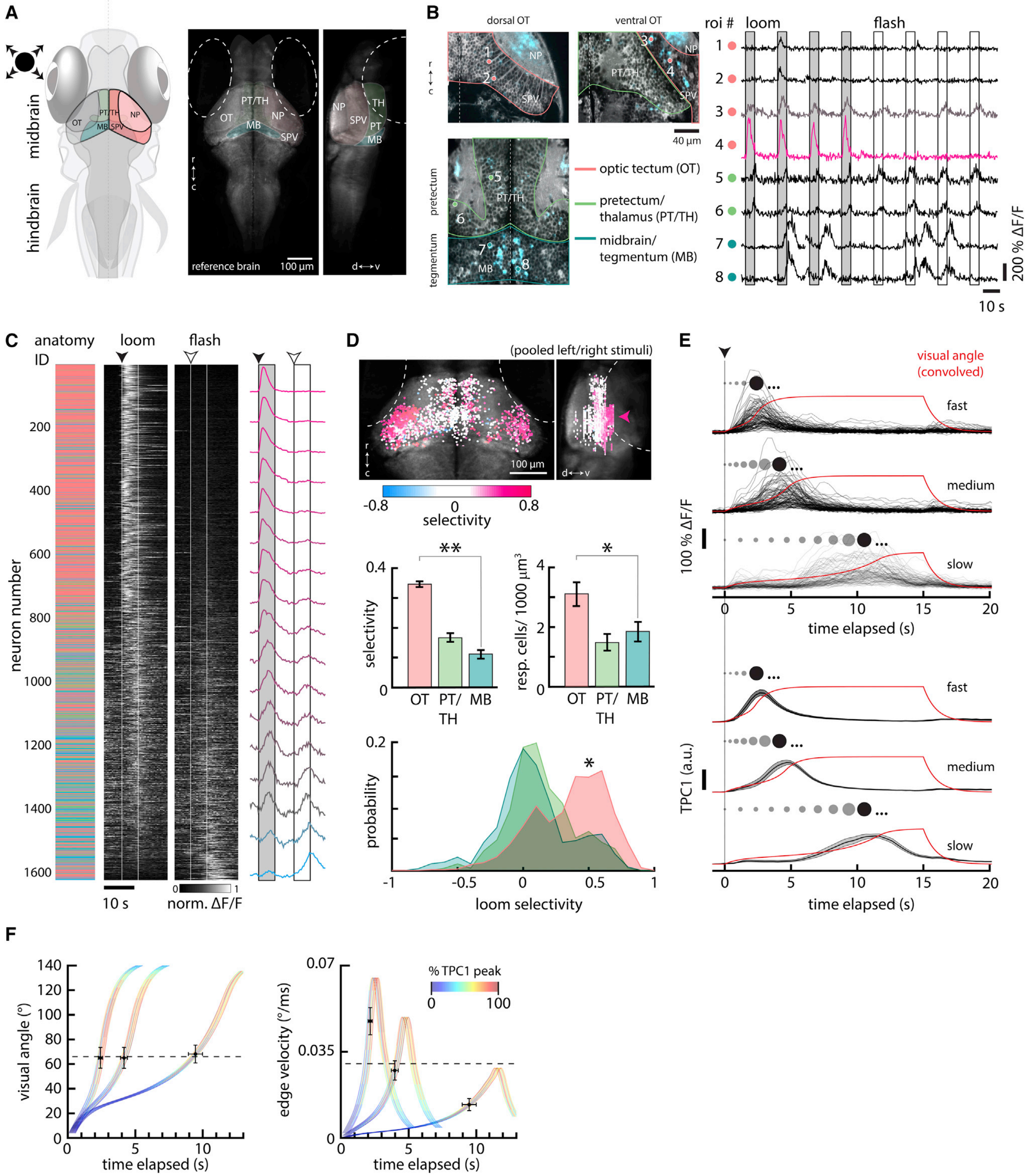

Figure 3. Looming-Specific Neurons in the Optic Tectum Encode Critical Size

(A) Left panel is a schematic of the larval zebrafish brain indicating the positions of the optic tectum (OT) with its neuropil (NP) and cell body layers (stratum periventriculare, or SPV), the pretectum/thalamus (PT/TH), and the midbrain tegmental region (MB). The right panels depict a transverse average intensity projection of a 5-dpf *Tg(elavl3:GCaMP2)* larval brain (used as an anatomical reference) and accompanying sagittal view. TH, thalamus; PT, pretectum. Dotted lines denote the position of each eye: r, rostral; c, caudal; d, dorsal; and v, ventral.

(legend continued on next page)

enhanced R^2 values, with three pairs, including the best model, properly incorporating SIN activity as inhibitory (Figure 5C). Of these three pairs, two share a common RGC type, and two share a common SIN type. Notably, the best model uses an RGC type (no. 1) that, on its own, explains PVN activity poorly (alone $R^2 = 0.22$, with SINs $R^2 = 0.89$), illustrating that SIN inhibition may contribute to PVN dynamics significantly. This fit is also better than that achieved with a linear regression ($R^2 = 0.79$) combining all four RGC types. Furthermore, the best RGC-SIN model uses the most frequent RGC type (no. 1) and SIN type (no. 1), suggesting that OT looming computations are salient and comprise fundamental functional units established by direct retinal excitation and indirect, processed retinal inhibition.

The Mauthner System Dictates Looming-Evoked Escape Direction

After looming stimuli are processed by the OT, the OT must recruit a specific motor program that completes the sensorimotor transformation (see proposed model, Figure 6A). In adult teleost fish, activity in the M-cell, a large hindbrain spinal projection neuron involved in mechanosensory escapes, is correlated with looming-evoked escapes (Preuss et al., 2006), and the M-cell receives projections from the OT on its ventral dendrite (Zottoli et al., 1987). Given this history and the kinematic similarities between the escape responses evoked by mechanosensory and looming stimuli, we hypothesized that the M-cell and its segmental homologs, morphologically and functionally similar neurons in rhombomeres 4 to 6 (Liu and Fetcho, 1999), would govern visually evoked escape behavior.

To test this hypothesis, we backfilled the hindbrain reticulospinal system (Huang et al., 2013; O'Malley et al., 1996) to label the M-cell and its homologs (MiD2 and MiD3) and target them for laser ablation with a two-photon microscope. A short (100-ms to 2-s), high-power (~100-mW at sample) laser pulse (Orger et al., 2008) was sufficient to cause a loss of cell morphology and fluorescence specific to the targeted neuron and not its labeled neighbors (Figure 6B). Because escape direction is lateralized and easily separated by left-right stimulus position, we performed unilateral ablations of the M-cell and its homologs, using the intact contralateral side as an internal control. Analysis of monocular looming-evoked escapes before and after unilateral ablation revealed a pronounced decrease in maximum turn angle (Figure 6C). Only escape responses contralateral to the ablated M-system (M-cell, MiD2, and MiD3) were perturbed (non-ablated side, pre 102.5° ± 3.6°, post 97.7° ± 3.5°, $p = 0.093$; ablated side, pre 99.1° ± 3.3°, post 71.8° ± 3.4°, $p = 0.002$, permutation test). This change is consistent with the laterality conferred by the descending axons of the M-system (Gahtan and O'Malley, 2003) and is not explained by non-specific perturbations of other spinal projection neurons such as the ventromedially located spinal projection neurons (Huang et al., 2013), which determine the direction of ipsilateral turns. As a result of this turn deficit, escape trajectories also changed (Figure 6D). However, the reduction in turn angle and trajectory was not concomitant with an obvious decrease in escape velocity or distance (Figure 6E). The turn deficit was confirmed on a fish-by-fish basis (Figure 6F), and cumulative distribution plots of maximum turn angle revealed a significant shift in turn angle for the ablated side across all events ($p < 10^{-5}$).

Other kinematic parameters such as escape duration (Figure 6G) remained unchanged for responses to both the non-ablated and ablated side, suggesting that an independent population of neurons may control the late phase of the visually evoked escape response. We also analyzed histograms of spontaneous turn angles, which were not significantly different post-

---

(B) Left panels depict single planes showing anatomy (gray) and activity (blue) in the dorsal and ventral OT, PT/TH, and MB. Individual region of interest (ROI) numbers (ROIs shown as colored circles) correspond to the traces on the right, which illustrate the general pattern of activity observed across midbrain visual areas in response to looming stimuli. Neurons in the dorsal OT (1 and 2) respond weakly to looming stimuli. Neurons in the ventral OT (3 and 4) show more varied responses but typically respond strongly to and favor looming stimuli. Neurons in PT/TH (5 and 6) respond to both looming and flashed stimuli. Neurons in MB (7 and 8) were typically active spontaneously and non-stimulus-locked. Boxes represent stimulus presentation periods. Traces are re-ordered and concatenated from longer recordings.

(C) The middle panels show trial-averaged normalized ΔF/F evoked by looming and flashed stimuli from 1,613 active neurons across 12 fish. Each neuron is sorted according to its selectivity index (see Experimental Procedures) in descending order (1 = looming exclusive, −1 = flash exclusive). The left-most panel shows the corresponding anatomical location of each neuron, color-coded as in (B). The right-most panel shows the average normalized ΔF/F binned across 100 neurons from the sorted list. Traces are normalized to [0 1] after trial averaging. Normalization values were skewed to the right (maximum 586.24% ΔF/F, minimum 21.02% ΔF/F, and skewness 1.28). Dotted lines and boxes represent stimulus presentation periods, with start times indicated by arrowheads.

(D) The top panel depicts all neurons from (C) mapped to a reference brain and colored according to selectivity index. Arrowhead shows the preponderance of looming-selective neurons in the ventral OT. Differences in the number of OT neurons between the left and right hemispheres reflects a sampling bias (data from stimuli presented in the left and right visual fields were pooled); most OT imaging was unilateral. The middle panel shows bar plots quantifying mean selectivity (left) and responsive cell density (right) across the OT ($n = 60$ imaging planes), PT ($n = 34$), and MB ($n = 44$). In the bottom panel, histograms show the distribution of looming selectivity across neurons in the OT ($n = 973$ cells), PT ($n = 279$), and MB ($n = 361$). $^{**}p < 10^{-5}$, $^{*}p < 0.01$, permutation test. N = 12 larvae. r, rostral; c, caudal; d, dorsal; and v, ventral.

(E) Top shows the responses of 110 OT neurons in one fish to looming stimuli simulating approach at three different velocities (R/V 545 ms, 1,090 ms, and 2,730 ms, top to bottom). The stimulus size (angle) over time for each condition, convolved with a calcium impulse response function (CIRF) ($\tau = 962$ ms), is shown in red. Bottom shows the first temporal principal component (TPC1, ± SEM across fish) averaged over eight fish, 1,533 neurons. The spots above each trace schematize the size of the looming stimulus before the TPC1 threshold (dark spot). Stimuli continue to expand (ellipses) until the end of the stimulus epoch.

(F) Quantifications of average convolved stimulus visual angle (left) and edge velocity (right) at TPC1 threshold times (81% TPC1 response after normalization to maximum across all stimulus conditions) for all three velocity conditions. The colored curves show the convolved stimulus size and edge velocity for each condition, fanned to show TPC1 dynamics for individual fish. Each color value corresponds to the normalized amplitude of TPC1 activity during expansion. Crosses show the average value of each stimulus variable at the TPC1 threshold for each velocity condition. Error bars are SEM for TPC1 threshold timing (horizontal) and respective stimulus variables (vertical) across fish. Dotted lines represent the mean visual angle and edge velocity at TPC1 threshold across all fish and conditions.

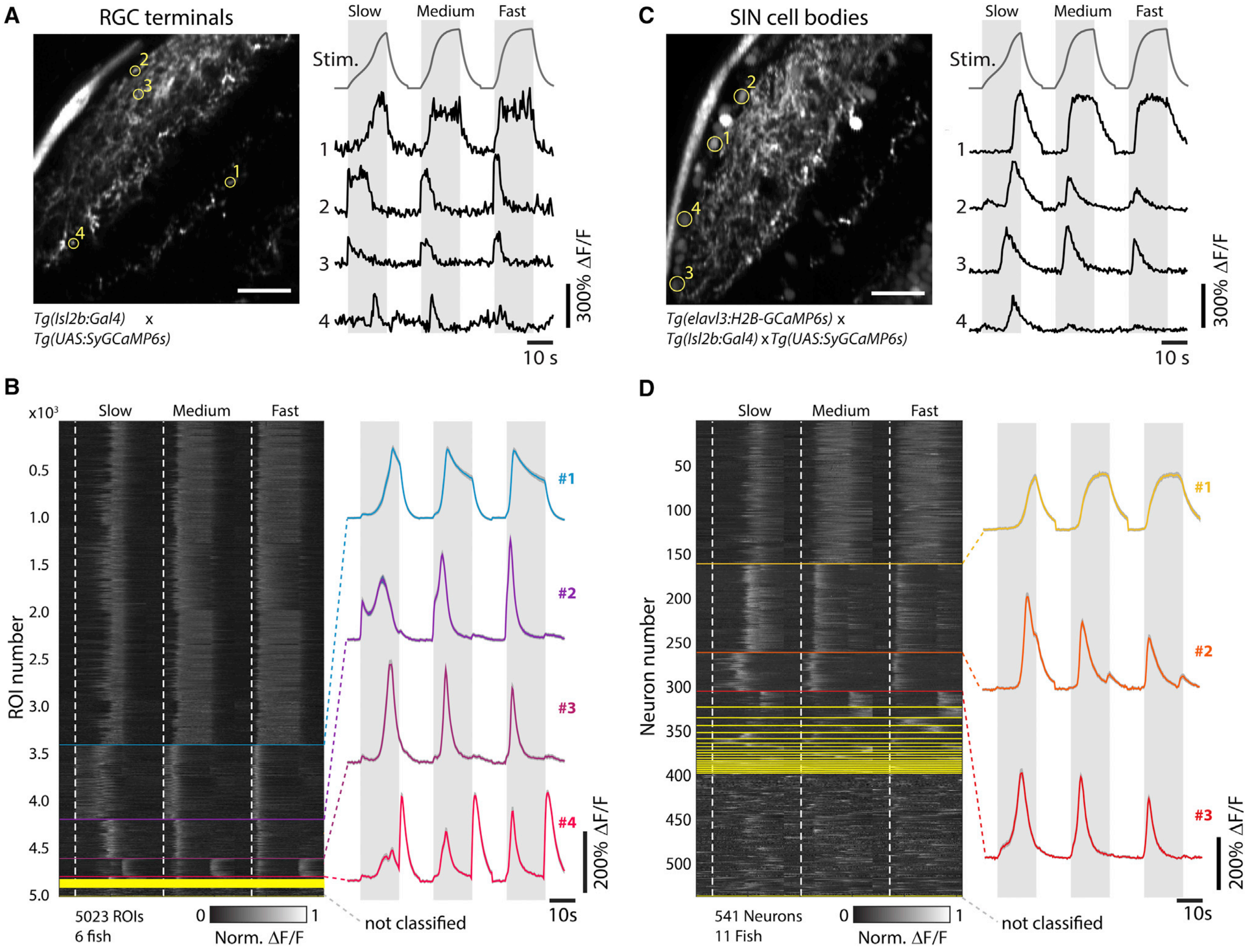

Figure 4. Retinotectal Processing of Looming Stimuli

(A) Left panel is a representative imaging plane from a 5-dpf *Tg(Isl2b:Gal4;UAS:SyGCaMP6s)* fish, which specifically expresses GCaMP6s in the axon terminals of RGCs. Scale bar, 20 μm. Right panel shows traces from the four ROIs indicated on the left (yellow circles), with convolved looming stimulus time courses for slow (R/V = 2,730 ms), medium (R/V = 1,090 ms), and fast (R/V = 545 ms) stimuli shown on top for reference. Gray intervals denote stimulus duration.

(B) Left panel is a raster plot after regression cluster analysis of normalized ΔF/F responses for n = 5,023 RGC terminal ROIs across N = 6 fish, sorted according to the number of individual traces assigned to each respective cluster. Start frames for each stimulus are denoted by the dotted white, vertical lines. Different clusters are separated by horizontal lines. The right panel shows mean traces of the four main clusters (containing at least 2% of the total ROIs from at least five fish, top to bottom: clusters 1–4, N = 3,420, 788, 413, and 192 ROIs, respectively).

(C) The left panel shows a representative imaging plane from a 5-dpf *Tg(elavl3:H2B-GCaMP6s;Isl2b:Gal4;UAS-SyGCaMP6s)* fish, which labels SINs. Scale bar, 20 μm. The right panel shows traces from the four ROIs indicated on the left (yellow circles).

(D) Left panel is a raster plot after regression cluster analysis of normalized ΔF/F responses for n = 541 SIN neurons across N = 11 fish, sorted according to the number of individual traces assigned to each respective cluster. Right panel shows mean traces of the three main clusters (containing at least 2% of the total neurons from at least eight fish, top to bottom: clusters 1–3, N = 163, 101, and 44 neurons, respectively).

ablation (Figure 6G, right). Because spontaneous turns are thought to be governed by separate premotor circuitry (Huang et al., 2013), we conclude that ablations were specific to the intended M-system targets.

These data provide strong evidence for multi-modal convergence of sensory signals within the M-system of larval zebrafish, and this is the first study to establish a necessary role of the M-system in visually evoked behavior. The M-system thus assumes an essential role in the sensorimotor transformation from looming stimuli to escape behavior, providing a functional scaffold for the zebrafish to quickly evade threats identified with their eyes alone.

DISCUSSION

We have shown, to the best our knowledge, the first quantification of visually evoked escape behavior in freely swimming larval zebrafish. This escape behavior is elicited specifically by looming stimuli and not by flashed or dimming spots, illustrating a highly tuned system for processing image expansion within the

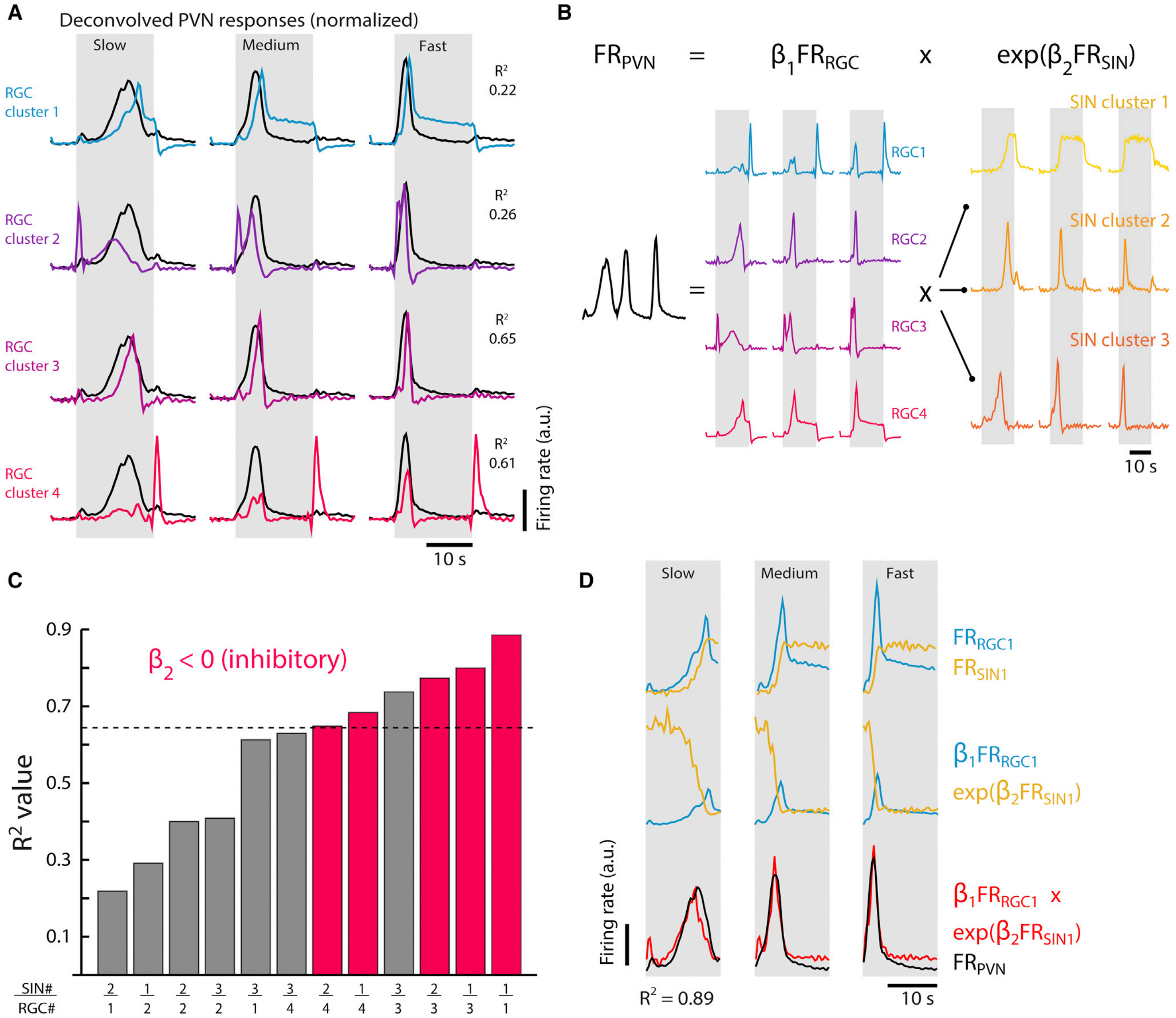

Figure 5. Regression Models Predict PVN Responses to Looming Stimuli

(A) Deconvolved mean RGC cluster traces (colored) overlaid on the deconvolved primary PVN trace (black; see Figure S4A, derived from the dataset in Figure 3E) collected in response to slow (R/V = 2,730 ms), medium (R/V = 1,090 ms), and fast (R/V = 545 ms) looming stimuli. R^2 values are calculating during stimulus period, gray. Each RGC trace is normalized to the maximum of the PVN trace across stimuli.

(B) Schematic of the eta-like non-linear regression model used to explore whether inhibition from SIN clusters can be combined with excitation from RGC clusters to tune PVN responses. The model attempts to explain the deconvolved firing rate of PVNs (FR_{PVN}) using a combination of scaled deconvolved RGC firing rate (FR_{RGC}) and exponentially weighted deconvolved SIN firing rate (FR_{SIN}), pairwise for each identified response cluster.

(C) Bar plot of the best-fit R^2 values for each SIN-RGC response pair, as determined by the non-linear regression in (B). Four combinations predict PVN responses better than the best-matched RGC cluster (black dotted horizontal line; $R^2 = 0.65$). Best-fit individual regression models that assign negative β_2 coefficients, and thus accurately treat GABAergic SINs as inhibitory, are shown in pink.

(D) Illustration of the best SIN-RGC regression model (right-most bar in C, $R^2 = 0.89$). The top traces show normalized FR_{RGC} (blue) and FR_{SIN} (gold) for clusters 1 and 1, respectively. The middle traces show individual model terms incorporating FR_{RGC} (blue) and FR_{SIN} (gold) and their respective best-fit coefficients. These traces are multiplied to arrive at a prediction of PVN activity (bottom, red). Note that FR_{RGC} is suppressed significantly by FR_{SIN} as stimuli increase in size, effectively shifting the FR_{RGC} peak to better match FR_{PVN} (bottom, black).

zebrafish visual system. High-angle turns elicited by whole-field dark flashes have been described previously (Burgess and Granato, 2007b; Chen and Engert, 2014; Huang et al., 2013), but these maneuvers ("o-bends") are relatively slow and are not followed by high-velocity burst swims. Furthermore, o-bend directionality appears linked to either turn history (Chen and Engert, 2014) or asymmetries in field luminance (Burgess and Granato, 2007b), not stimulus position. Thus, the dark flash response

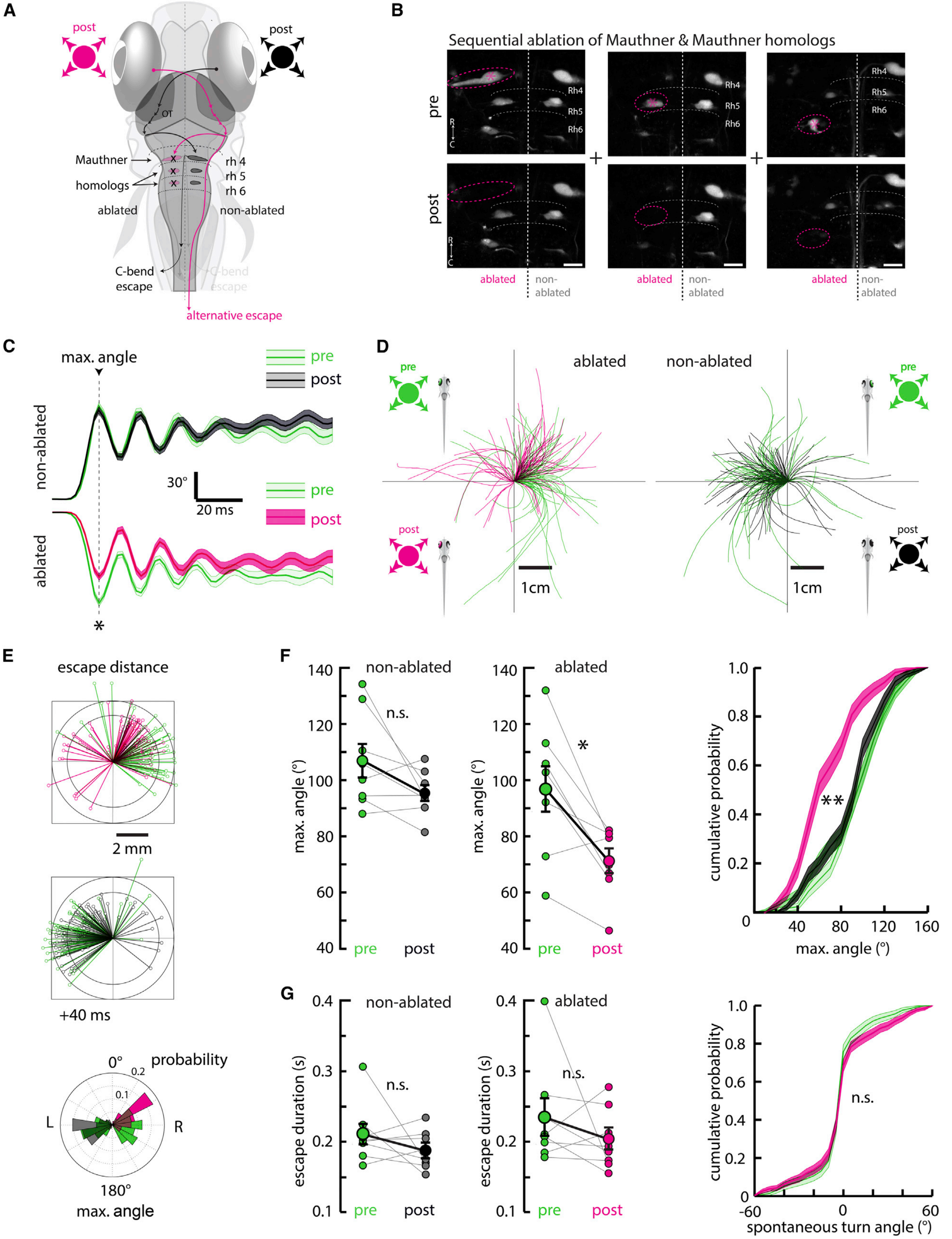

(legend on next page)

appears more to re-orient larvae than to propel them away from harm. Given these differences, we believe that looming-evoked escapes represent a separate, novel class of visually evoked behavior in larval zebrafish.

Analysis of the relationship between escape latency and approach velocity under our experimental conditions revealed a threshold angular image size for behavior initiation that is reminiscent of looming size thresholds in other organisms (Fotowat and Gabbiani, 2011; Oliva et al., 2007). In locusts and flies, the link between stimulus dynamics and behavior has been traced to a pair of wide-field neurons whose spike rates during looming can be described by a function (typically labeled *eta*) that peaks with a fixed delay before a critical visual angle (Hatsopoulos et al., 1995) and the onset of escape (Fotowat and Gabbiani, 2007). We provide evidence that a similar non-linear computation involves primary RGC and SIN types, but the specific way in which these components are combined to affect population activity in the OT is, as of yet, unknown.

In order to gain additional insight into the specific neural computation underlying looming detection, we functionally imaged main retino-recipient midbrain structures as they responded to looming and flashed stimuli and uncovered a preponderance of looming-selective neurons within the ventrocaudal OT. This selectivity may be conferred by the integration of motion-selective inputs from the retina (Nikolaou et al., 2012) or from within the OT itself (Gabriel et al., 2012; Grama and Engert, 2012). Although we have not assessed the necessity of the OT for looming-evoked escapes, the high density of looming-selective responses in the ventrocaudal OT provides strong correlative evidence that the OT is involved in processing looming stimuli; extra-tectal neurons and arborization fields may process other visual cues such as whole-field motion and luminance changes. Given the broad responsiveness of neurons within the OT and the nature of our stimulus delivery (onto the dorsal retina), it is likely that the concentration of looming selectivity in the ventrocaudal OT arises primarily due to established retinotopy (Nevin et al., 2010) and does not reflect a specialized processing region. However, the broad spatial distribution of activity within the OT, along with our principal component analysis, does suggest that the computation and isolation of looming-related features from the visual scene may operate at a network level before activity is projected out of the OT to recruit downstream motor programs.

Although it remains possible that a subset of looming-selective neurons in the OT form a specialized class of looming detectors that drive behavior, a distributed representation of critical visual angle presents several distinct advantages. First, the majority of tectal neuron spatial receptive fields (as assayed by moving spots) are smaller than the critical image size that appears to trigger the escape behavior (Niell and Smith, 2005). Large stimuli may thus be encoded best by a combination of multiple tectal neurons staggered over retinotopic space. Second, a distributed representation of stimuli may increase the overall flexibility of stimulus representation in the OT. Because animals must extract relevant information from complex visual scenes occupying a large space of possible stimulus combinations, a functional platform for encoding many different stimuli across the OT population can guide behavior more amenably. The ensemble encoding of critical visual angle during stimulus expansion thus constitutes a small subset of the total response space likely spanned by the OT. Last, high-dimensional representations of stimuli have been shown to improve animal performance on tasks by increasing the degeneracy of available input-output relationships in readout neurons (Rigotti et al., 2013). It is possible that the escape circuitry presented here utilizes a similar strategy to ensure that escapes are triggered reliably in individual animals and across stimulus presentations.

We have shown that the OT population representation of looming stimuli may require distinct computational modules that contribute uniquely to the encoding of critical visual angle during stimulus expansion. GCaMP6s expression in RGC presynaptic boutons allowed us to measure RGC activity patterns in response to looming stimuli. We used these patterns to construct a model predicting that OT ensemble activity is

Figure 6. Laser Ablation of the Mauthner System Alters Escape Trajectory and Reduces Initial Bend Angle

(A) Schematic of the zebrafish brain and hypothesized information flow from the eye, through the contralateral OT, to the contralateral hindbrain Mauthner system (M-system) comprising the Mauthner cell (M-cell) and homologs in rhombomeres 4–6.

(B) Two-photon micrographs showing an example of the M-cell (left), MiD2 (center), and MiD3 (right) pre- and post-unilateral ablation. For each fish, the M-cell and MiD2/MiD3 clusters were ablated together. Ablations were specific to targeted neurons and did not affect nearby cells. Cells were backfilled with dextran-conjugated dye. Scale bar is 20 μm.

(C) The average maximum turn angle derived from orientation change, see Experimental Procedures, during escapes is significantly altered for maneuvers contralateral to the ablated side, with the largest change evident at the first (maximum) bend. The average escape ipsilateral to the ablated side remained unchanged. All traces are aligned to the time point of the first bend. Error is SEM across all events, N = 8 fish. Pre, non-ablated, n = 60 events; pre, ablated, n = 73; post, non-ablated, n = 88; post, ablated, n = 66. $^*p = 0.002$, permutation test.

(D) Left panel shows escape trajectories pre- and post-ablation (green and pink, respectively) elicited by stimuli ipsilateral to the ablated side. Right panels shows escape trajectories pre- and post-ablation (green and black, respectively) elicited by stimuli contralateral to the ablated side.

(E) Top panel shows stick diagrams representing fish position 40 ms after escape initiation for the ablated and non-ablated sides, pre- and post-ablation. The shift in escape trajectory post-ablation is more apparent on this timescale. Bottom panel is an angular histogram of the maximum turn angle pre- and post-ablation for the ablated and non-ablated sides.

(F) Left panel shows quantification of maximum turn angle across fish pre- and post-ablation for the ablated and non-ablated sides. $^*p = 0.002$, n.s., $p = 0.093$, permutation test. Right panel shows that this change is also apparent in histograms of maximum turn angle across all events; $^{**}p < 10^{-5}$ ablated side, $p = 0.175$ non-ablated side, permutation test across all events. Error is bootstrapped SEM.

(G) Left panel shows quantification of escape duration. No significant change is apparent on either side after ablation. Non-ablated, $p = 0.073$. Ablated, $p = 0.101$, permutation test. Error bars are SEM across fish. Right panel shows the distribution of spontaneous turns does not change after ablation, providing further evidence of ablation specificity; pre-ablation n = 744, post-ablation n = 911 spontaneous swim events; n.s., $p = 0.725$, permutation test. Error is bootstrapped SEM.

generated through a modulation of one class of RGC inputs by a specific subset of SINs that may act individually, but also in concert, to shape the population code across PVNs. These PVNs could then innervate the M-cell via synapses that might further be gated or modulated by independent or parallel inputs. The experiments reported here thus provide a framework for a quantitative model of looming selectivity, whose precise details remain to be identified by future experiments.

A recent study analyzed looming-evoked behavior in head-restrained zebrafish larvae (Temizer et al., 2015) and found that escapes are elicited by expanding dark or bright disks in the visual field. Consistent with our study, the authors discovered a size threshold for the behavior, albeit of a value different from our own observations (21.7° visual angle). This discrepancy probably results from differences in experimental conditions (i.e., head-restrained side-projection versus freely swimming bottom-projection); future analyses, such as consideration of visual solid angle and Snell's law (Wolf and Krötzsch, 1995), should help reconcile these results. In addition, Temizer et al. show that RGC arbors in the stratum fibrosum et griseum superficiale (SFGS) of the OT are selective for looming over dimming stimuli. We show, however, that simply integrating over RGCs is insufficient to explain the time course of the PVN dynamics correlated with critical angle. Rather, we suggest that further intratectal processing via interneurons in the upper layers of the OT is necessary.

Last, we sought to shed light on the involvement of the M-cell in the context of looming-evoked escapes. While canonical C-start escape responses are preceded by a spike in the M-cell, ablation of the M-system only affects escape latency and bend velocity, not bend angle, when assayed with acoustic or tactile stimuli (Burgess and Granato, 2007a; Liu and Fetcho, 1999). These results have cemented an idea of parallel hindbrain escape circuitries that form a redundant pathway for escape behavior. However, ablation of the M-system results in a specific bend deficit in response to looming stimuli, suggesting that visual stimuli recruit only a subset of the available escape circuitry, perhaps reflecting a functional bias toward more reliable modalities (e.g., mechanosensation). How the escape circuitry receives signals from visual areas to trigger an escape is still unclear, however. Anatomical and functional evidence from adult goldfish has suggested a direct pathway from the OT to the ventral dendrite of the M-cell (Zottoli et al., 1987), but this pathway has yet to be confirmed in larval zebrafish, leaving open the possibility of either a direct or indirect path from the OT. Taken together, our study provides an overview of a potential circuit mediating a visually evoked escape behavior in a vertebrate model organism and provides an important foundation for future studies of ethologically relevant tectal processing.

EXPERIMENTAL PROCEDURES

Behavior

All experiments followed the guidelines of the National Institutes of Health and were approved by the Standing Committee on the Use of Animals in Research of Harvard University. For detailed kinematic analyses, larvae (5–6 dpf) were monitored at 506 fps using a high-speed camera (Mikrotron GmbH) in a 9.2-cm Petri dish (VWR), 3–5 mm water height. Custom-written C# software extracted fish position and orientation and updated stimuli in a closed-loop configuration. For constant radial expansion trials, the stimulus was centered 0.5 cm to either the left or right of the fish center of mass. Stimuli expanded with a constant radial velocity of 0.5 or 0.6 cm/s until reaching r = 1 cm and disappeared 5 s after expansion commenced. Stimuli were presented onto a screen underneath the fish using a digital light processing (DLP) projector (Dell M109S).

Calcium Imaging

To assay neural responses, 5- to 6-dpf *Tg(elavl3:GCaMP5G)* larvae (Ahrens et al., 2013) were paralyzed with alpha-bungarotoxin (1 mg/mL; Invitrogen) and embedded in 2% low-melting-point agarose before being imaged with a custom-built two-photon laser scanning microscope. Stimuli were presented in the red channel onto a screen underneath the fish using a digital light processing (DLP) projector (Dell M109S).

For more details regarding behavior analyses, imaging analyses, ablations, and statistics, see Supplemental Experimental Procedures.

SUPPLEMENTAL INFORMATION

Supplemental Information includes Supplemental Experimental Procedures, four figures, and two movies and can be found with this article online at http://dx.doi.org/10.1016/j.neuron.2015.12.021.

AUTHOR CONTRIBUTIONS

T.W.D., M.B.A., F.E., and F.D.B. conceived the project; T.W.D. carried out the experiments and analyzed the data; C.G. analyzed data and conceived the SIN experiments. C.R. generated transgenic fish lines. T.W.D., C.G., E.A.N., M.B.A., F.E., and F.D.B. wrote the paper.

ACKNOWLEDGMENTS

We are grateful to James Fitzgerald for aiding in the initial analysis of the imaging data and to Jeremy Freeman for providing advice on statistical analysis. We thank Drew Robson, Jennifer Li, and Michael Orger for generating the *Tg(elavl3-GCaMP5G)* fish line. We thank Jessica Miller, Steve Zimmerman, and Alex Schier for fish husbandry. We thank Evan Feinberg, Arjun Krishnaswamy, Joseph Bell, Isaac Bianco, and Christopher Harvey for providing helpful feedback on the manuscript. T.W.D. was supported by the National Science Foundation Graduate Research Fellowship Program, and his collaboration with C.G. and F.D.B. was made possible by the NSF Graduate Research Opportunities Worldwide Fellowship. E.A.N. was supported by a Marie Curie fellowship. F.D.B. was supported by an ATIP/AVENIR-program starting grant and by ERC-StG no. 311159, CNRS, INSERM, and Institut Curie core funding. We thank the Developmental Biology Curie imaging facility (PICT-IBiSA@BDD, Paris, France, UMR3215/U934), member of the France-BioImaging national research infrastructure, for their help with microscopy. The Del Bene laboratory "Neural Circuits Development" is part of the Laboratoire d'Excellence (LABEX) entitled DEEP (ANR-11-LABX-0044) and of the École des Neurosciences de Paris Ile-de-France network. C.G. was supported by a postdoctoral fellowship from the Fondation pour la Recherche Médicale (FRM).

Received: September 22, 2014
Revised: July 20, 2015
Accepted: December 3, 2015
Published: January 21, 2016

REFERENCES

Ahrens, M.B., Li, J.M., Orger, M.B., Robson, D.N., Schier, A.F., Engert, F., and Portugues, R. (2012). Brain-wide neuronal dynamics during motor adaptation in zebrafish. Nature *485*, 471–477.

Ahrens, M.B., Orger, M.B., Robson, D.N., Li, J.M., and Keller, P.J. (2013). Whole-brain functional imaging at cellular resolution using light-sheet microscopy. Nat. Methods *10*, 413–420.

Armstrong, P.B., and Higgins, D.C. (1971). Behavioral encephalization in the bullhead embryo and its neuroanatomical correlates. J. Comp. Neurol. *143*, 371–384.

Baranauskas, G., Svirskiene, N., and Svirskis, G. (2012). 20Hz membrane potential oscillations are driven by synaptic inputs in collision-detecting neurons in the frog optic tectum. Neurosci. Lett. *528*, 196–200.

Bianco, I.H., and Engert, F. (2015). Visuomotor transformations underlying hunting behavior in zebrafish. Curr. Biol. *25*, 831–846.

Bianco, I.H., Kampff, A.R., and Engert, F. (2011). Prey capture behavior evoked by simple visual stimuli in larval zebrafish. Front. Syst. Neurosci. *5*, 101.

Billington, J., Wilkie, R.M., Field, D.T., and Wann, J.P. (2011). Neural processing of imminent collision in humans. Proc. Biol. Sci. *278*, 1476–1481.

Budick, S.A., and O'Malley, D.M. (2000). Locomotor repertoire of the larval zebrafish: swimming, turning and prey capture. J. Exp. Biol. *203*, 2565–2579.

Burgess, H.A., and Granato, M. (2007a). Sensorimotor gating in larval zebrafish. J. Neurosci. *27*, 4984–4994.

Burgess, H.A., and Granato, M. (2007b). Modulation of locomotor activity in larval zebrafish during light adaptation. J. Exp. Biol. *210*, 2526–2539.

Burrill, J.D., and Easter, S.S., Jr. (1994). Development of the retinofugal projections in the embryonic and larval zebrafish (Brachydanio rerio). J. Comp. Neurol. *346*, 583–600.

Card, G., and Dickinson, M.H. (2008). Visually mediated motor planning in the escape response of Drosophila. Curr. Biol. *18*, 1300–1307.

Chalfie, M., Sulston, J.E., White, J.G., Southgate, E., Thomson, J.N., and Brenner, S. (1985). The neural circuit for touch sensitivity in Caenorhabditis elegans. J. Neurosci. *5*, 956–964.

Chen, X., and Engert, F. (2014). Navigational strategies underlying phototaxis in larval zebrafish. Front. Syst. Neurosci. *8*, 39.

Chen, T.-W., Wardill, T.J., Sun, Y., Pulver, S.R., Renninger, S.L., Baohan, A., Schreiter, E.R., Kerr, R.A., Orger, M.B., Jayaraman, V., et al. (2013). Ultrasensitive fluorescent proteins for imaging neuronal activity. Nature *499*, 295–300.

de Vries, S.E.J., and Clandinin, T.R. (2012). Loom-sensitive neurons link computation to action in the Drosophila visual system. Curr. Biol. *22*, 353–362.

Dean, P., Redgrave, P., and Westby, G.W. (1989). Event or emergency? Two response systems in the mammalian superior colliculus. Trends Neurosci. *12*, 137–147.

Del Bene, F., Wyart, C., Robles, E., Tran, A., Looger, L., Scott, E.K., Isacoff, E.Y., and Baier, H. (2010). Filtering of visual information in the tectum by an identified neural circuit. Science *330*, 669–673.

Dickinson, M., and Moss, C.F. (2012). Neuroethology. Curr. Opin. Neurobiol. *22*, 177–179.

Domenici, P., Booth, D., Blagburn, J.M., and Bacon, J.P. (2008). Cockroaches keep predators guessing by using preferred escape trajectories. Curr. Biol. *18*, 1792–1796.

Dunn, O.J. (1961). Multiple comparisons among means. J. Am. Stat. Assoc. *56*, 52–64.

Eaton, R.C., and Emberley, D.S. (1991). How stimulus direction determines the trajectory of the Mauthner-initiated escape response in a teleost fish. J. Exp. Biol. *161*, 469–487.

Eaton, R.C., DiDomenico, R., and Nissanov, J. (1988). Flexible body dynamics of the goldfish C-start: implications for reticulospinal command mechanisms. J. Neurosci. *8*, 2758–2768.

Eaton, R.C., Lee, R.K., and Foreman, M.B. (2001). The Mauthner cell and other identified neurons of the brainstem escape network of fish. Prog. Neurobiol. *63*, 467–485.

Ewert, J.P. (1997). Neural correlates of key stimulus and releasing mechanism: a case study and two concepts. Trends Neurosci. *20*, 332–339.

Fotowat, H., and Gabbiani, F. (2007). Relationship between the phases of sensory and motor activity during a looming-evoked multistage escape behavior. J. Neurosci. *27*, 10047–10059.

Fotowat, H., and Gabbiani, F. (2011). Collision detection as a model for sensory-motor integration. Annu. Rev. Neurosci. *34*, 1–19.

Fotowat, H., Harrison, R.R., and Gabbiani, F. (2011). Multiplexing of motor information in the discharge of a collision detecting neuron during escape behaviors. Neuron *69*, 147–158.

Freeman, J., Vladimirov, N., Kawashima, T., Mu, Y., Sofroniew, N.J., Bennett, D.V., Rosen, J., Yang, C.-T., Looger, L.L., and Ahrens, M.B. (2014). Mapping brain activity at scale with cluster computing. Nat. Methods *11*, 941–950.

Gabbiani, F., Krapp, H.G., and Laurent, G. (1999). Computation of object approach by a wide-field, motion-sensitive neuron. J. Neurosci. *19*, 1122–1141.

Gabbiani, F., Mo, C., and Laurent, G. (2001). Invariance of angular threshold computation in a wide-field looming-sensitive neuron. J. Neurosci. *21*, 314–329.

Gabriel, J.P., Trivedi, C.A., Maurer, C.M., Ryu, S., and Bollmann, J.H. (2012). Layer-specific targeting of direction-selective neurons in the zebrafish optic tectum. Neuron *76*, 1147–1160.

Gahtan, E., and O'Malley, D.M. (2003). Visually guided injection of identified reticulospinal neurons in zebrafish: a survey of spinal arborization patterns. J. Comp. Neurol. *459*, 186–200.

Gahtan, E., Sankrithi, N., Campos, J.B., and O'Malley, D.M. (2002). Evidence for a widespread brain stem escape network in larval zebrafish. J. Neurophysiol. *87*, 608–614.

Grama, A., and Engert, F. (2012). Direction selectivity in the larval zebrafish tectum is mediated by asymmetric inhibition. Front. Neural Circuits *6*, 59.

Hatsopoulos, N., Gabbiani, F., and Laurent, G. (1995). Elementary computation of object approach by wide-field visual neuron. Science *270*, 1000–1003.

Huang, K.-H., Ahrens, M.B., Dunn, T.W., and Engert, F. (2013). Spinal projection neurons control turning behaviors in zebrafish. Curr. Biol. *23*, 1566–1573.

Humphries, D.A., and Driver, P.M. (1970). Protean defence by prey animals. Oecologia *5*, 285–302.

Hunter, P.R., Lowe, A.S., Thompson, I.D., and Meyer, M.P. (2013). Emergent properties of the optic tectum revealed by population analysis of direction and orientation selectivity. J. Neurosci. *33*, 13940–13945.

Khakhalin, A.S., Koren, D., Gu, J., Xu, H., and Aizenman, C.D. (2014). Excitation and inhibition in recurrent networks mediate collision avoidance in Xenopus tadpoles. Eur. J. Neurosci. *40*, 2948–2962.

Kohashi, T., and Oda, Y. (2008). Initiation of Mauthner- or non-Mauthner-mediated fast escape evoked by different modes of sensory input. J. Neurosci. *28*, 10641–10653.

Kohashi, T., Nakata, N., and Oda, Y. (2012). Effective sensory modality activating an escape triggering neuron switches during early development in zebrafish. J. Neurosci. *32*, 5810–5820.

Korn, H., and Faber, D.S. (2005). The Mauthner cell half a century later: a neurobiological model for decision-making? Neuron *47*, 13–28.

Kubo, F., Hablitzel, B., Dal Maschio, M., Driever, W., Baier, H., and Arrenberg, A.B. (2014). Functional architecture of an optic flow-responsive area that drives horizontal eye movements in zebrafish. Neuron *81*, 1344–1359.

Landwehr, K., Brendel, E., and Hecht, H. (2013). Luminance and contrast in visual perception of time to collision. Vision Res. *89*, 18–23.

Liu, K.S., and Fetcho, J.R. (1999). Laser ablations reveal functional relationships of segmental hindbrain neurons in zebrafish. Neuron *23*, 325–335.

Muijres, F.T., Elzinga, M.J., Melis, J.M., and Dickinson, M.H. (2014). Flies evade looming targets by executing rapid visually directed banked turns. Science *344*, 172–177.

Muto, A., Ohkura, M., Abe, G., Nakai, J., and Kawakami, K. (2013). Real-time visualization of neuronal activity during perception. Curr. Biol. *23*, 307–311.

Nevin, L.M., Robles, E., Baier, H., and Scott, E.K. (2010). Focusing on optic tectum circuitry through the lens of genetics. BMC Biol. *8*, 126.

Niell, C.M., and Smith, S.J. (2005). Functional imaging reveals rapid development of visual response properties in the zebrafish tectum. Neuron *45*, 941–951.

Nikolaou, N., Lowe, A.S., Walker, A.S., Abbas, F., Hunter, P.R., Thompson, I.D., and Meyer, M.P. (2012). Parametric functional maps of visual inputs to the tectum. Neuron *76*, 317–324.

O'Malley, D.M., Kao, Y.-H., and Fetcho, J.R. (1996). Imaging the functional organization of zebrafish hindbrain segments during escape behaviors. Neuron *17*, 1145–1155.

Oliva, D., Medan, V., and Tomsic, D. (2007). Escape behavior and neuronal responses to looming stimuli in the crab Chasmagnathus granulatus (Decapoda: Grapsidae). J. Exp. Biol. *210*, 865–880.

Orger, M.B., Kampff, A.R., Severi, K.E., Bollmann, J.H., and Engert, F. (2008). Control of visually guided behavior by distinct populations of spinal projection neurons. Nat. Neurosci. *11*, 327–333.

Portugues, R., Feierstein, C.E., Engert, F., and Orger, M.B. (2014). Whole-brain activity maps reveal stereotyped, distributed networks for visuomotor behavior. Neuron *81*, 1328–1343.

Preuss, T., Osei-Bonsu, P.E., Weiss, S.A., Wang, C., and Faber, D.S. (2006). Neural representation of object approach in a decision-making motor circuit. J. Neurosci. *26*, 3454–3464.

Preuss, S.J., Trivedi, C.A., vom Berg-Maurer, C.M., Ryu, S., and Bollmann, J.H. (2014). Classification of object size in retinotectal microcircuits. Curr. Biol. *24*, 2376–2385.

Rigotti, M., Barak, O., Warden, M.R., Wang, X.-J., Daw, N.D., Miller, E.K., and Fusi, S. (2013). The importance of mixed selectivity in complex cognitive tasks. Nature *497*, 585–590.

Santer, R.D., Yamawaki, Y., Rind, F.C., and Simmons, P.J. (2005). Motor activity and trajectory control during escape jumping in the locust Locusta migratoria. J. Comp. Physiol. A Neuroethol. Sens. Neural Behav. Physiol. *191*, 965–975.

Sherrington, C.S. (1910). Flexion-reflex of the limb, crossed extension-reflex, and reflex stepping and standing. J. Physiol. *40*, 28–121.

Temizer, I., Donovan, J.C., Baier, H., and Semmelhack, J.L. (2015). A visual pathway for looming-evoked escape in larval zebrafish. Curr. Biol. *25*, 1823–1834.

Vanegas, H., and Ito, H. (1983). Morphological aspects of the teleostean visual system: a review. Brain Res. *287*, 117–137.

von Reyn, C.R., Breads, P., Peek, M.Y., Zheng, G.Z., Williamson, W.R., Yee, A.L., Leonardo, A., and Card, G.M. (2014). A spike-timing mechanism for action selection. Nat. Neurosci. *17*, 962–970.

Winkowski, D.E., and Knudsen, E.I. (2008). Distinct mechanisms for top-down control of neural gain and sensitivity in the owl optic tectum. Neuron *60*, 698–708.

Wolf, K.B., and Krötzsch, G. (1995). Geometry and dynamics in refracting systems. Eur. J. Phys. *16*, 14–20.

Yilmaz, M., and Meister, M. (2013). Rapid innate defensive responses of mice to looming visual stimuli. Curr. Biol. *23*, 2011–2015.

Zottoli, S.J., Hordes, A.R., and Faber, D.S. (1987). Localization of optic tectal input to the ventral dendrite of the goldfish Mauthner cell. Brain Res. *401*, 113–121.